A Generalization of the Double-Corner-Frequency Source Spectral Model and Its Use in the SCEC BBP Validation Exercise

by David M. Boore, Carola Di Alessandro, and Norman A. Abrahamson

Abstract   The stochastic method of simulating ground motions requires the specification of the shape and scaling with magnitude of the source spectrum. The spectral models commonly used are either single-corner-frequency or double-corner-frequency models, but the latter have no flexibility to vary the high-frequency spectral levels for a specified seismic moment. Two generalized double-corner-frequency ω^2 source spectral models are introduced, one in which two spectra are multiplied together and another where they are added. Both models have a low-frequency dependence controlled by the seismic moment and a high-frequency spectral level controlled by the seismic moment and a stress parameter. A wide range of spectral shapes can be obtained from these generalized spectral models, which makes them suitable for inversions of data to obtain spectral models that can be used in ground-motion simulations in situations in which adequate data are not available for purely empirical determinations of ground motions, such as in stable continental regions. As an example of the use of the generalized source spectral models, data from up to 40 stations from seven events, plus response spectra at two distances and two magnitudes from recent ground-motion prediction equations, were inverted to obtain the parameters controlling the spectral shapes, as well as a finite-fault factor that is used in point-source, stochastic-method simulations of ground motion. The fits to the data are comparable to or even better than those from finite-fault simulations, even for sites close to large earthquakes.

Introduction

The stochastic method is widely used to simulate ground motions at frequencies of engineering interest (e.g., Hanks and McGuire, 1981; Boore, 2003). The essence of the method is to assume that the energy from an earthquake is spread over a duration that is a function of the source size and the propagation distance. The Fourier spectrum of the motion is assumed to be given by an amplitude spectrum based on a seismological model, with essentially random phase (the phase is not strictly random because the time-domain duration is finite). The key to the success of the method is in specifying the frequency-domain Fourier acceleration amplitude spectrum (FAS). The FAS is usually made up of multiplicative components, sometimes referred to as filters, representing the source and the propagation path. The path effects include changes of amplitude due to geometrical spreading, attenuation due to intrinsic attenuation and scattering, and amplification of the motion as the waves travel though material in which the seismic velocity generally decreases from the source to the Earth's surface, as well as any near-site amplifications. The various components of the FAS can be given by seismological theory with parameters often set by purely empirical observations. This article focuses on the source com-

ponent of the stochastic method. The simplest and most commonly used source is the classic single-corner-frequency (SCF) ω^2 model (e.g., Brune, 1970, 1971). Ignoring multiplicative constants, the FAS (for brevity, we now use A rather than FAS) is given by

$$A \propto \frac{M_0 f^2}{1 + (f/f_c)^2}, \qquad (1)$$

in which M_0 is the seismic moment and f_c is the corner frequency (see Boore, 1983, 2003, for a complete description of the FAS). The source acceleration spectrum is flat at frequencies sufficiently above the corner frequency, with the high-frequency level A_{HF} being given by

$$A_{\mathrm{HF}} \propto M_0 f_c^2. \qquad (2)$$

The corner frequency can be related to the seismic moment M_0 (or equivalently, moment magnitude **M**) and a parameter $\Delta\sigma$ having the units of stress by this equation:

$$f_c = 4.906 \times 10^6 \beta (\Delta\sigma/M_0)^{1/3}, \qquad (3)$$

in which β is the shear-wave velocity in the vicinity of the source. The units of f_c, β, $\Delta\sigma$, and M_0 in this equation are Hz, km/s, bars, and dyn·cm, respectively.

The stochastic method has been implemented in the software package Stochastic-Method SIMulation (SMSIM; Boore, 2005). In that software, a number of source models more complicated than the SCF model have also been included. All of the source models are point-source models, in that no information regarding the dimensions or orientation of the rupture surface is used in the simulations. Finite-fault effects, such as modifications to the spectral shape (e.g., a spectrum with a sag between two corner frequencies, as has been observed in a number of earthquakes; see Boore, 1986, and references therein) and the reduction of amplitudes due to motions arriving from parts of the fault at distances larger than the closest distance to the site, are approximated by suitable choices of the source-spectral model and the source-to-site distance. The more complicated source models all have two corner frequencies (f_a and f_b) rather than a single corner frequency (f_c), and they all have a flat high-frequency acceleration spectrum. The change of amplitude with source size can be described conveniently by the dependence of f_a and f_b on moment magnitude (e.g., tables 2 and 3 in Boore, 2003). With only one exception (Joyner, 1984; source model 2 in SMSIM), A_{HF} in the published double-corner models is fixed for a given M_0. The main purpose of this article is to introduce two models for which A_{HF} can vary for a given M_0, thus introducing more flexibility in fitting source models to data. In one model the spectra involving f_a and f_b are multiplicative, and in the other they are additive; we call these generalized double-corner-frequency (DCF) source models. The basic motivation for using a generalized DCF model is that data from a number of earthquakes suggest that it is better than an SCF model, and the generalization allows more flexibility in fitting data from a given earthquake.

We illustrate the use of the additive generalized DCF source models in the project to validate the Southern California Earthquake Center's Broadband Platform (SCEC BBP) simulation methods (D. S. Dreger *et al.*, unpublished report, 2014; C. A. Goulet *et al.*, unpublished report, 2014; see Data and Resources). This is the second published use of the additive generalized DCF source model, the first being by Yenier and Atkinson (2014), who used a completely different scheme for fitting the model to the observations. The observations themselves were different (vertical component FAS for Yenier and Atkinson; horizontal component pseudoabsolute response spectral acceleration [PSA] for the BBP study), and the earthquakes providing the data only overlapped slightly (two earthquakes were in common, out of seven for the BBP study and eleven for Yenier and Atkinson, 2014). For the SCEC BBP validation exercise, additional data were also provided for two magnitudes from recent ground-motion predictions equations (GMPEs) those magnitudes are within the magnitude range of the events used in the Yenier and Atkinson (2014) study. We conclude the article with some provisional relations between one of the parameters

related to the source spectrum and the adjustment of the distance used in the point-source calculations that might be used in future applications (forward modeling) of the point-source stochastic model.

Generalization of Double-Corner-Frequency Source Models Used in SMSIM

The basic constraints of the generalized DCF source model are that the acceleration spectrum should increase as f^2 at low frequencies, with an amplitude proportional to the seismic moment, and that the spectrum should be flat at high frequencies, with an amplitude equal to that of an SCF source model with a specified $\Delta\sigma$. In this section, we provide equations for generalizing DCF models to allow the high-frequency source spectral level to be determined by the stress parameter $\Delta\sigma$ (the basic idea being that the DCF source model will have the same high-frequency source spectral level as an SCF source model with a specified $\Delta\sigma$). We discuss first the multiplicative double-corner-frequency (MDCF) model and then the additive double-corner-frequency (ADCF) model.

Generalized MDCF Source Spectrum

Let the acceleration source spectrum be proportional to

$$A \propto M_0 f^2 \frac{1}{[1 + (f/f_a)^{\mathrm{pf}_a}]^{\mathrm{pd}_a}} \frac{1}{[1 + (f/f_b)^{\mathrm{pf}_b}]^{\mathrm{pd}_b}}, \quad (4)$$

in which pf and pd stand for power of frequency and power of denominator. The subscripts a and b refer to quantities appearing in the two parts of the double-corner-frequency source models. For high frequencies ($f \gg f_a$ and $f \gg f_b$), this becomes

$$A_{HF} \propto \frac{M_0 f^2}{f^{(\mathrm{pf}_a \times \mathrm{pd}_a + \mathrm{pf}_b \times \mathrm{pd}_b)}} f_a^{\mathrm{pf}_a \times \mathrm{pd}_a} f_b^{\mathrm{pf}_b \times \mathrm{pd}_b}. \quad (5)$$

The constancy of the high-frequency acceleration spectral level requires that the following constraint be satisfied:

$$\mathrm{pf}_a \times \mathrm{pd}_a + \mathrm{pf}_b \times \mathrm{pd}_b = 2. \quad (6)$$

If this constraint is satisfied, then the powers pf and pd can be related to an equivalent stress parameter and SCF model, as follows. For an SCF model with corner frequency f_c, the high-frequency spectral level is given in equation (2). Equating equations (2) and (5), with the constraint given by equation (6), gives

$$f_c^2 = f_a^{\mathrm{pf}_a \times \mathrm{pd}_a} f_b^{\mathrm{pf}_b \times \mathrm{pd}_b}. \quad (7)$$

The procedure then is to use equation (3) to obtain f_c, given β, $\Delta\sigma$, and M_0, in which M_0 comes from moment magnitude **M** using the relation

$$\log M_0 = 1.5\mathbf{M} + 16.05 \quad (8)$$
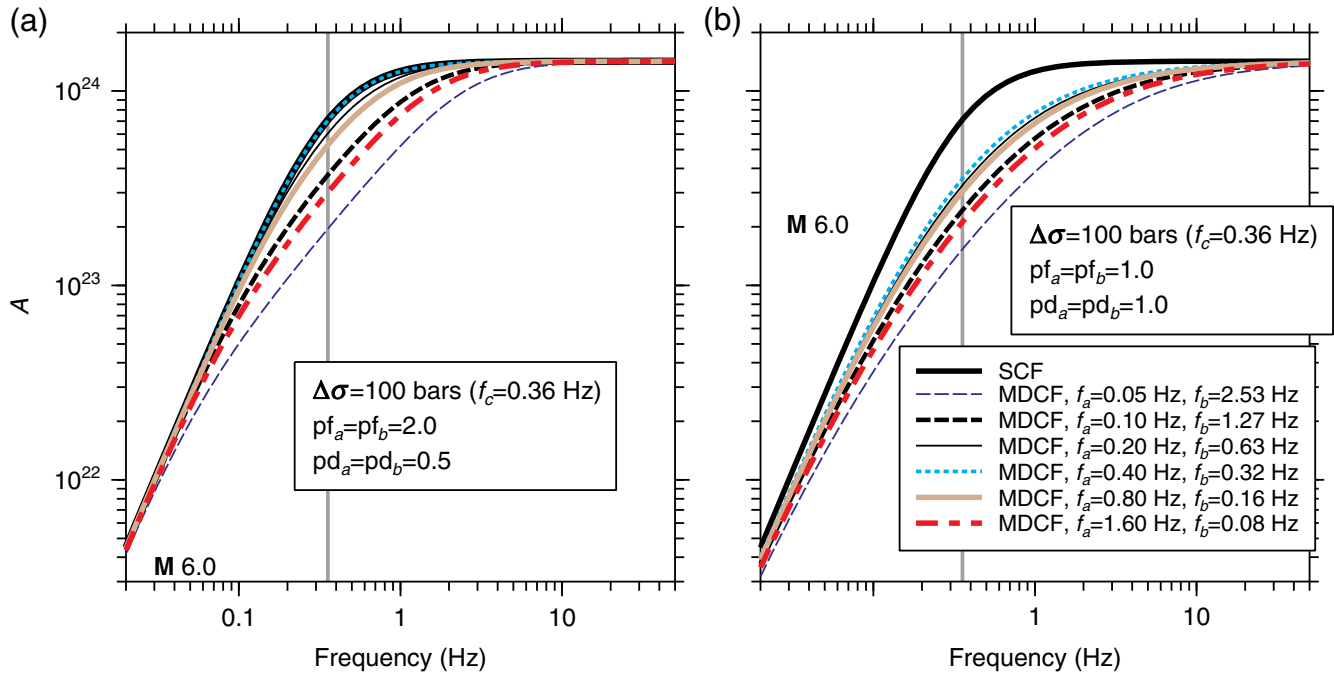
Figure 1. Source spectra for the multiplicative double-corner-frequency (MDCF) source model for different choices of the powers of frequency and of the denominators (the values of pf_a, pf_b, pd_a, and pd_b are given in the legends of panels a and b), for a series of f_a values, **M** 6, and a single value of $\Delta\sigma$. Also shown is the spectrum and corner frequency (gray vertical line) for the single-corner-frequency (SCF) source model. The MDCF model in (a) is the same as the SCF model when $f_a = 0.356$ Hz, rounded to 0.36 in the figure, but the source spectrum for this value of f_a is virtually indistinguishable from that for $f_a = 0.400$ Hz, as shown by the coincidence of the dotted and heavy curves. The color version of this figure is available only in the electronic edition.

(Hanks and Kanamori, 1979). Assuming that f_a is specified by the user, then equation (7) can be used to find f_b:

$$f_b = \left[\frac{f_c^2}{f_a^{pf_a \times pd_a}}\right]^{1/(pf_b \times pd_b)}. \tag{9}$$

There are no numerical restrictions on the values of f_a and f_b or on their relative sizes. We illustrate this model for two sets of the powers pf_a, pd_a, pf_b, and pd_b, both sets satisfying the constraints in equation (6). In the first example, $pf_a = pf_b = 2$ and $pd_a = pd_b = 0.5$. Figure 1a shows the source spectra for this model, assuming $\mathbf{M} = 6$ and $\Delta\sigma = 100$ bars, for a series of f_a. With these choices of the powers, the MDCF sources merge into the SCF model when $f_a = f_c = 0.36$ Hz, as expected from the formulation above. In contrast, Figure 1b shows the source spectra for $pf_a = pf_b = pd_a = pd_b = 1.0$, and in this case, the MDCF model never approaches the SCF model.

Generalized ADCF Source Spectrum

Let the acceleration source spectrum be proportional to

$$A \propto \frac{M_0 f^2 (1-\varepsilon)}{[1 + (f/f_a)^{pf_a}]^{pd_a}} + \frac{M_0 f^2 \varepsilon}{[1 + (f/f_b)^{pf_b}]^{pd_b}}, \tag{10}$$

in which ε is a weighting parameter giving the relative contributions of the two SCF spectra; we attribute no physical

meaning to the parameter. The first author proposed this source model to G. Atkinson (personal comm., 1992), and she used it to derive a source spectral model for eastern North American earthquakes (Atkinson, 1993). This form of the source model was subsequently used in other papers by Atkinson and her colleagues (e.g., Atkinson and Boore, 1995; Atkinson and Silva, 2000). For high frequencies ($f \gg f_a$ and $f \gg f_b$), equation (10) becomes

$$A_{\mathrm{HF}} \propto \left(\frac{M_0 f^2}{f^{pf_a \times pd_a}}\right)(1-\varepsilon)f_a^{pf_a \times pd_a} + \left(\frac{M_0 f^2}{f^{pf_b \times pd_b}}\right)\varepsilon f_b^{pf_b \times pd_b}. \tag{11}$$

For a flat high-frequency acceleration spectrum, the constraint

$$pf_a \times pd_a = pf_b \times pd_b = 2, \tag{12}$$

must be satisfied, and the high-frequency level is

$$A_{\mathrm{HF}} \propto M_0(1-\varepsilon)f_a^2 + M_0\varepsilon f_b^2. \tag{13}$$

If the constraint in equation (12) is satisfied, then equating the high-frequency source spectral level to the level for an SCF model gives
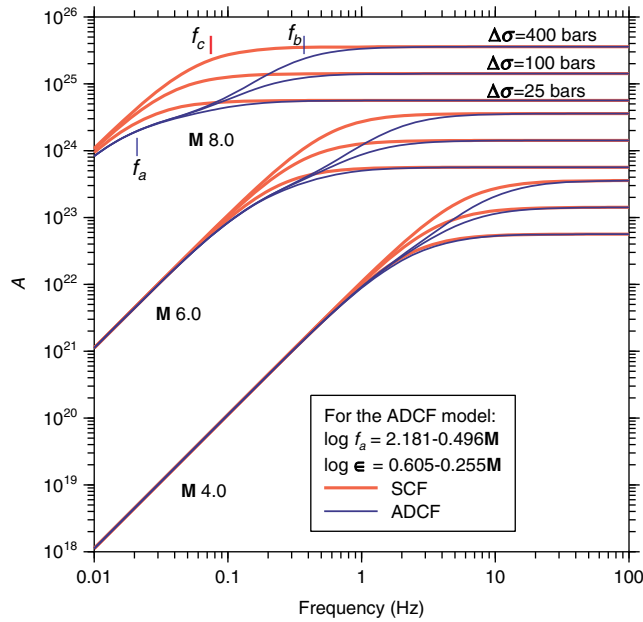
Figure 2. Source spectra for the additive double-corner-frequency (ADCF) source model, for a series of magnitudes **M** and stress parameters $\Delta\sigma$. The $\log f_a$ and $\log \varepsilon$ relations are from Atkinson and Silva (2000). Also shown are the spectra for the SCF source model. The corner frequencies for the ADCF source model (f_a and f_b) and the SCF source model (f_c) are shown for **M** = 8 and $\Delta\sigma$ = 400 bars. The color version of this figure is available only in the electronic edition.

$$f_b = f_a \sqrt{\frac{(f_c/f_a)^2 - (1 - \varepsilon)}{\varepsilon}}. \qquad (14)$$

This then generalizes the ADCF model by letting the high-frequency level be determined by a stress parameter $\Delta\sigma$.

In applications of the generalized ADCF source model, equation (3) is used to obtain f_c, given $\Delta\sigma$ and M_0. Assuming that f_a and ε are specified by the user, such as in the following ways:

$$\log f_a = c_{1fa} + c_{2fa}(\mathbf{M} - \mathbf{M}_{fa}) \qquad (15)$$

and

$$\log \varepsilon = c_{1\varepsilon} + c_{2\varepsilon}(\mathbf{M} - \mathbf{M}_{\varepsilon}) \qquad (16)$$

(e.g., the $\log f_a$ and $\log \varepsilon$ relations of Atkinson and Silva, 2000; these are given in the legend in Fig. 2). Equation (14) then is used to determine f_b. The natural range of ε is between 0 and 1 (although this is not a strict requirement), and we will assume this to be the case from here on. For this range, there will be a value of $\Delta\sigma$ below which f_b is not defined for a given f_a and **M**. This occurs when the numerator under the radical in equation (14) equals 0.0. From equations (3) and (14), the lower limit for $\Delta\sigma$ is

$$\Delta\sigma_{\min} = \left[\frac{\sqrt{1 - \varepsilon}}{\xi} f_a\right]^3 M_0, \qquad (17)$$
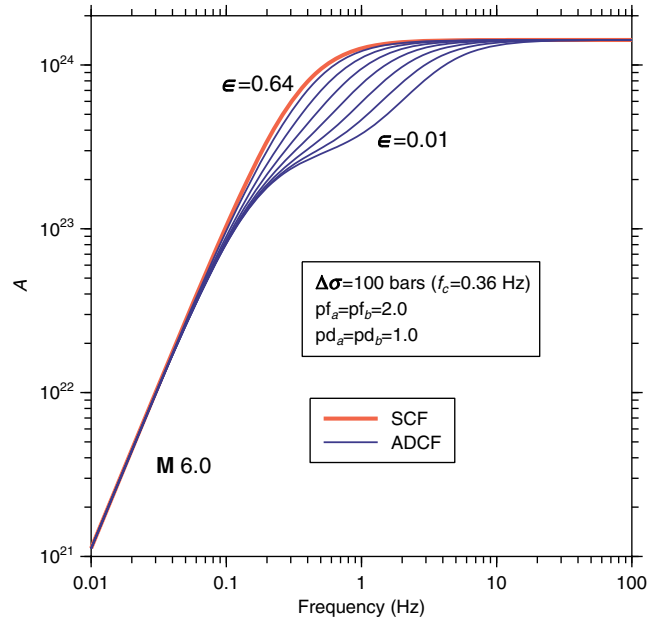
Figure 3. Source spectra for the ADCF source model, for a series of ε, **M** = 6, and $\Delta\sigma$ = 100 bars. f_a = 0.16 Hz, from Atkinson and Silva (2000). Also shown is the spectrum for the SCF source model. The color version of this figure is available only in the electronic edition.

in which

$$\xi = 4.906 \times 10^6 \beta. \qquad (18)$$

(The units of f_c, β, $\Delta\sigma$, and M_0 implied by this equation are given below equation 3). Although equation (17) gives the minimum value of $\Delta\sigma$ for a specified M_0 and f_a, it does not guarantee anything about the relative sizes of the three corner frequencies. Although there is nothing that requires a certain order of the frequencies, we note that the condition $f_a < f_c$ is satisfied if $\Delta\sigma$ is any value greater than the $\Delta\sigma_{\min}$ given by evaluating equation (17) with $\varepsilon = 0.0$. Even with this condition, however, f_b can be less than either f_a or f_c, depending on the choice of the free parameters $\Delta\sigma$, ε, and f_a.

To illustrate the flexibility of the model, Figure 2 shows source spectra for the ADCF source model for several values of **M** and $\Delta\sigma$, compared with the SCF source model. As required by the formulation, the SCF and ADCF models have the same high-frequency spectral levels for the same value of the stress parameter. We used $pf_a = pf_b = 2.0$ and $pd_a = pd_b = 1.0$ for the example in this and subsequent figures. For the f_a and ε relations used in the figure (from Atkinson and Silva, 2000), the ADCF model has a significant spectral sag at intermediate frequencies. The extent of this sag can be controlled by the parameter ε, as shown in Figure 3. That figure shows the source spectra for a suite of ε values differing by a factor of 2, ranging from 0.01 to 0.64, for a specified value of f_a.

As an example of the ADCF model, we simulated the motions at 10 km for an **M** 6 earthquake, with an effective

(a)

(b)
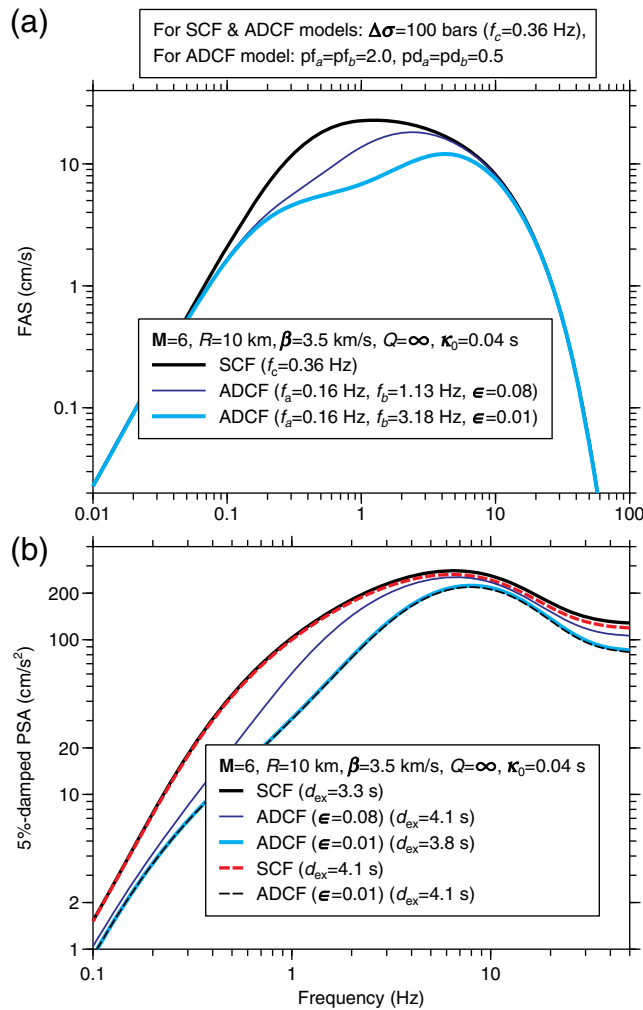
Figure 4. Fourier acceleration amplitude spectrum (FAS) and pseudoabsolute response spectral acceleration (PSA) for **M** = 6, $R = 10$ km, $\Delta\sigma = 100$ bars, and $\kappa_0 = 0.04$ s. For the ADCF model two values of ε were used: 0.01 and 0.08. f_a was computed from the equation in Atkinson and Silva (2000). The PSAs shown by solid curves are for excitation durations (d_{ex}) composed of the source duration for each model (see text) plus a path duration of 0.5 s. To show the importance of differences in duration, the dashed curves show the results when the path durations have been adjusted to give the same excitation durations (4.1 s) for each model. The color version of this figure is available only in the electronic edition.

SCF stress parameter of 100 bars. Two values of ε, 0.01 and 0.08, were used for the ADCF model. Figure 4 shows the Fourier and corresponding response spectra for the SCF and the ADCF models. Unlike the FAS, the PSA for the SCF and the ADCF source models are never in agreement, even for frequencies for which the FAS agree, with the PSA from the ADCF model always being below that of the PSA from the SCF model. One reason for the differences in the PSA is that different source durations were used for the models. For the SCF source, the duration was given by $1/f_c$ (e.g., equation 3 in Hanks and McGuire, 1981), whereas for the ADCF source model, the source duration used in the simulations is given by $0.5/f_a + 0.5/f_b$. The result for this example is that the
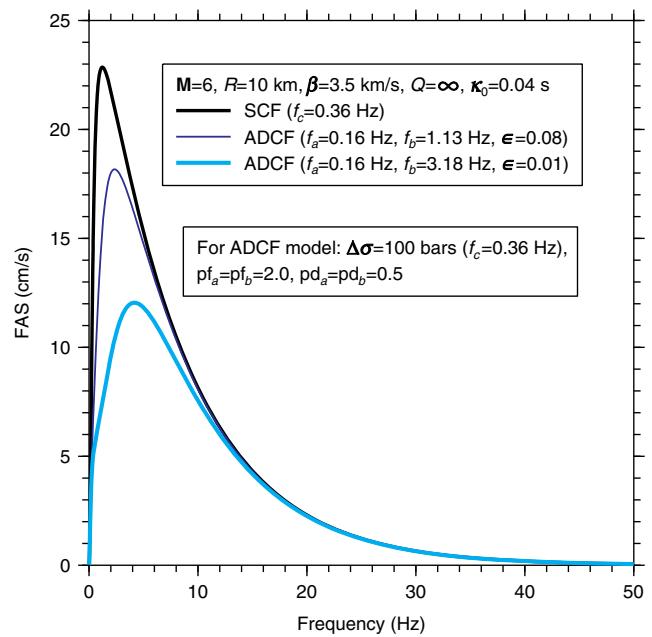
Figure 5. The FAS shown in Figure 4, plotted using linear axes. The color version of this figure is available only in the electronic edition.

source duration equals 2.8 s for the SCF model and 3.3 and 3.6 s for the ADCF models with ε equal to 0.01 and 0.08, respectively. Adding the assumed path duration of 0.5 s yields total duration of excitation (d_{ex}) of 3.3, 3.8, and 4.1 s for the three models, as shown in the figure legend. To isolate the effect on response spectra of excitation duration from differences in the shape of the FAS, we adjusted the path durations so that all models had the same excitation duration (equal to the longest unadjusted duration, corresponding to the ADCF model with $\varepsilon = 0.08$). The results are shown by the dashed lines in Figure 4. These lines show that duration has only a small effect. Of greatest importance are the differences in the shapes of the FAS. Recalling that the levels of response spectra at long and short periods are not related to the FAS at those periods, but rather are proportional to the ground motion at periods that control the peak displacement and peak acceleration, it is no surprise that the response spectra for the three models differ significantly at long and short periods. To emphasize this, Figure 5 shows the FAS that is included in Figure 4 but plotted using linear axes. We do this because the peak acceleration is closely related to the root mean square (rms) acceleration, which is given by the square root of the integral of the squared FAS over linear frequency. It is obvious from Figure 5 that the three models will have different rms values, and thus different peak accelerations and different short-period response spectra (which are proportional to the peak accelerations).

As an aside, the equation for the ADCF source duration in the previous paragraph differs from that used in Atkinson and Boore (1995) and Atkinson and Silva (2000); they use $0.5/f_a + 0.0/f_b$. The problem with this source duration is

Table 1
Parameters Obtained from Inverting the Data from Parts A and B of the SCEC BBP Validation Exercise

Part	Event	Year	M (BBP)	M (NGA-West 2)	Mechanism*	$\Delta\sigma$ (bars)[†]	$\Delta\sigma'$ (bars)[‡]	h (km)	ϵ
A	Landers	1992	7.22	7.28	SS	100	90	22.38	0.020
A	Loma Prieta	1989	6.94	6.93	ROS	150	153	15.85	0.043
A	Northridge	1994	6.73	6.69	RS	100	107	0.50	0.077
A	North P.S.	1986	6.12	6.02	ROS	175	208	11.22	0.068
A	Whittier	1987	5.89	5.99	ROS	200	168	7.94	0.125
A	Niigta	2004	6.65	6.63	RS	175	181	2.80	0.005
A	Tottori	2000	6.59	6.61	SS	150	145	22.38	0.052
B	**M** 6.2, SS	—	6.20	6.20	SS	100	100	9.12	0.140
B	**M** 6.6, SS	—	6.60	6.60	SS	85	85	12.02	0.110
B	**M** 6.6, RS	—	6.60	6.60	RS	95	95	12.02	0.085

*Mechanisms: SS, strike slip; RS, reverse slip; ROS, reverse-oblique slip.
[†]$\Delta\sigma$ is the stress parameter from the inversion, using the SCEC BBP magnitude given by **M** (BBP)
[‡]$\Delta\sigma'$ is the adjusted stress parameter, using equation (20) and the magnitude given by **M** (NGA-West 2).

that it leads to a discontinuity in duration at the magnitude for which the two corner frequencies become equal, if it is assumed that $f_a = f_b$ for magnitudes less than that magnitude. For these smaller magnitudes, the usual assumption would be that the duration equals $1.0/f_a$. We prefer using equal weights of 0.5 for both inverse corner frequencies, as this avoids the discontinuity. In addition, as magnitude increases, f_b generally increases much more rapidly than f_a, and as a result the duration is primarily controlled by the term $0.5/f_a$, which is the equation used by Atkinson and Boore (1995) and Atkinson and Silva (2000).

An Example of Using the Generalized DCF Source Model: Application in the SCEC BBP Validation Exercise

We now address an application of the ADCF source model in a multiyear, intensive project known as the SCEC BBP validation exercise (see C. A. Goulet *et al.*, unpublished report, 2014, see Data and Resources, for a discussion of the project design and execution). The primary goal of the BBP exercise was to test various finite-fault simulation methods against data from a number of earthquakes in a carefully controlled study for which the data to be used and the constraints on the model parameters used in the methods were carefully prescribed. The project was composed of two parts: part A consisted of comparing simulations to available records recorded by up to 40 stations at distances within 200 km for seven earthquakes in the 5.9–7.2 magnitude range, and part B compared simulations to PSA values from a number of recent GMPEs for two magnitudes, two distances, and different style-of-faulting mechanisms (reverse and strike slip) for which the response spectra are well determined from numerous recordings (referred to as the scenario events). (See D. S. Dreger *et al.*, unpublished report, 2014, see Data and Resources, for the results of the BBP validation exercise.) A list of the events and scenarios used in the BBP exercise is given in Table 1. Although the BBP exercise was focused in finite-fault simulation methods, the point-source stochastic model, as de-

scribed by Boore (2003) and implemented by the software package SMSIM (Boore, 2005), was used for comparison with the more complex finite-fault simulation methods.

Source-Parameter Determinations for the SCEC BBP Validation Exercise Events

We used Raoof *et al.* (1999) geometrical spreading and Q. The crustal amplification function was obtained using the square-root impedance approach (Boore, 2013) applied to a reference velocity profile derived for the SCEC BBP validation exercise. The shear-wave velocity decreased from 3.5 km/s near the source to a time-weighted average shear-wave velocity over the upper 30 m of 863 m/s. The reference crustal profile was obtained by interpolation of the two profiles for western North America ($V_{S30} = 618$ m/s) and central and eastern North America ($V_{S30} = 2880$ m/s) given in Boore and Joyner (1997), such that $V_{S30} = 863$ m/s (see Data and Resources). The amplifications are given in Table 2. The density and shear-wave velocity at the source were 2.72 g/cm^3 and 3.5 km/s, respectively, and the average radiation pattern was 0.55. All of the parameters given above were kept fixed and were not adjusted to fit the data for each event.

Preliminary analyses using the SCF and the two DCF source models showed that the SCF model was not capable of reproducing the observed motions. Although values of $\Delta\sigma$ could be found that provided a fit to the observed response spectra at short periods, the simulations from the SCF source model consistently overestimated the response at longer periods. In addition, the greater flexibility in the spectral shape of the ADCF source model compared with the MDCF source model allowed for a better match to the target spectra. For those reasons, we used the ADCF source model for the exercise. We used the Atkinson and Silva (2000) relation between f_a and **M**, and we inverted for $\Delta\sigma$ and ϵ for each event. We also determined a finite-fault factor h that is used to adjust the closest distance from the rupture surface to the site (R_{RUP}), using the equation

Table 2
Crustal Amplifications (with No Attenuation)

Frequency (Hz)	Amplification
0.010	0.321
0.015	0.440
0.021	1.015
0.031	1.022
0.046	1.033
0.067	1.049
0.098	1.074
0.144	1.113
0.210	1.164
0.308	1.224
0.450	1.291
0.659	1.368
0.964	1.459
1.411	1.569
2.065	1.714
3.022	1.881
4.422	2.053
6.472	2.220
9.470	2.377
13.859	2.548
20.280	2.733
29.677	2.936
43.429	3.155
63.552	3.392
93.000	3.635

Figure 6. The average residuals, the 90% confidence limits of the residuals, and ±1 standard deviation of the residuals for records from 40 stations that recorded the 1992 **M** 7.3 Landers earthquake. The longest period used in the inversion for the source parameters was 3 s. The heavy vertical black line indicates the period beyond which there were fewer than three observations to use in computing the mean bias and its associated uncertainty. The color version of this figure is available only in the electronic edition.

$$R = \sqrt{R_{\mathrm{RUP}}^2 + h^2}. \qquad (19)$$

The distance used in the point-source simulations is R. Equation (19) accounts for finite-fault effects in the point-source model. This is an essential modification to the point-source model, as discussed in a number of papers (e.g., Atkinson and Silva, 2000; Toro, 2002; Boore, 2009; Boore, 2014; Yenier and Atkinson, 2014). A grid search was used to solve for h, $\Delta\sigma$, and ε for each event (the results are included in Table 1). Reasonable ranges for the unknowns were used, and a penalty function was designed that gave joint consideration to the mean bias between the observed and the simulated response spectra over a period range extending from short periods to a period of 3 s and to the trend of the residuals with distance. Based on numerous comparisons of simulated and target spectra, the attenuation parameter κ_0 (Hough *et al.*, 1988) was set to 0.035 s for all events but Tottori (for which $\kappa_0 = 0.02$ s).

Some results for individual events are shown in Figures 6–8 for the part A events and Figure 9 for one part B scenario event. The figures for the part A events show the goodness of fit (GOF), defined as the ratio of the observed to simulated motions, or ln(obs/sim). This GOF measure is computed independently for each spectral period for up to 40 selected stations. Figure 6 is an example of a typical fit over the period range of the inversion (out to 3 s), with an underprediction for longer periods (something that is true for several of the other events), whereas Figures 7 and 8 show the best and worst fits out of the seven part A validation events. The good agreement between target and simulated

PSA for the part B scenario events is shown in Figure 9. Although not shown here, comparably good agreement was obtained for the other scenario events.

Looking for Trends in the Source Parameters

Although the results shown in Figures 6–9 demonstrate that the point-source stochastic method with the ADCF source model and a finite-fault adjustment factor has adequate flexibility to reproduce observed data, it is important to see if the values of h, $\Delta\sigma$, and ε determined for each event (Table 1) show any systematic trends with **M**. If they did, then the trends could be used in simulations of ground motions for future events. Figure 10 shows h, $\Delta\sigma$, and ε inversions of the SCEC BBP validation exercise events. Recall that the part A parameters were determined from many stations (up to 40) for each event, whereas for part B they are for the PSA at two magnitudes and distances for which the motions are well constrained by the data from a large number of recordings. As such, the parameters from part B may lead to better-calibrated values of the ADCF source parameters and to values that would be more useful in predictions of median ground motions for future events than for the few individual events used in part A.

The graph of $\Delta\sigma$ in Figure 10 suggests that, on average, the part A events have a higher stress parameter than implied by the GMPEs (part B). As there are some differences in the **M** values used in the SCEC BBP validation exercise for part A
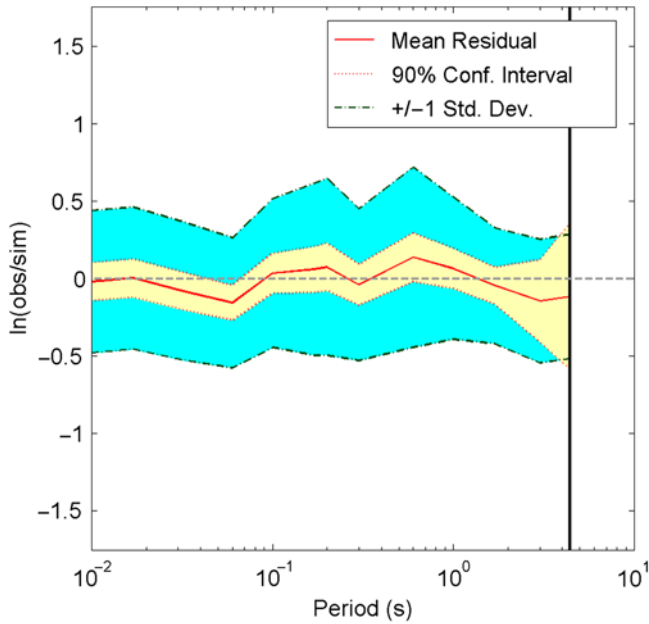
Figure 7. The average residuals, the 90% confidence limits of the residuals, and ±1 standard deviation of the residuals for records from 39 stations that recorded the 1987 **M** 6.0 Whittier Narrows earthquake. The longest period used in the inversion for the source parameters was 3 s. The heavy vertical black line indicates the period beyond which there were fewer than three observations to use in computing the mean bias and its associated uncertainty. The color version of this figure is available only in the electronic edition.
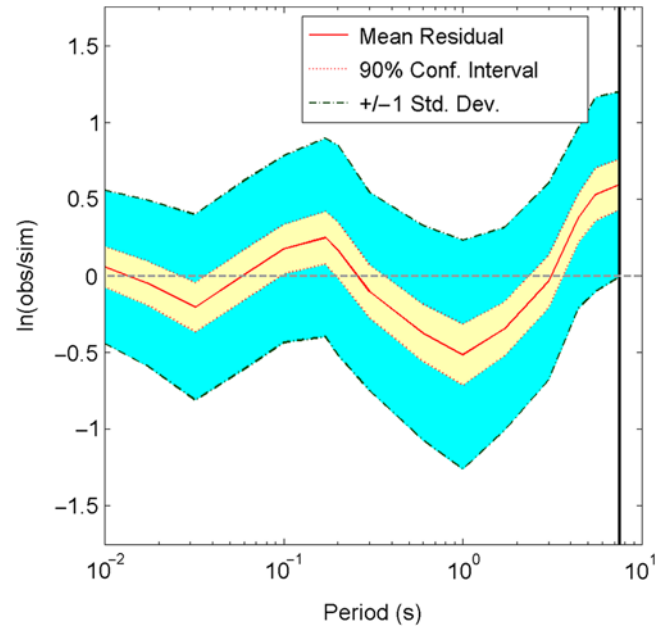
Figure 8. The average residuals, the 90% confidence limits of the residuals, and plus and minus one standard deviation of the residuals for records from 40 stations that recorded the 2000 **M** 6.6 Tottori earthquake. The longest period used in the inversion for the source parameters was 3 s. The heavy vertical black line indicates the period beyond which there were fewer than three observations to use in computing the mean bias and its associated uncertainty. The color version of this figure is available only in the electronic edition.

and those in the Pacific Earthquake Engineering Research Center Next Generation Attenuation-West 2 (NGA-West 2) database (we used the NGA-West 2 magnitudes in Fig. 10), we adjusted the inverted $\Delta\sigma$ values from part A to be consistent with the **M** in the figure. The adjustments were made using the equation

$$\Delta\sigma_1/\Delta\sigma_2 = 10^{0.75(\mathrm{M}_2-\mathrm{M}_1)}. \tag{20}$$

This equation is based on the constraint that the high-frequency spectral levels should be the same for any $\Delta\sigma$, **M** pair. Equation (20) was derived using equations (2), (3), and (8). Considering the $\Delta\sigma$ obtained from parts A and B separately, there is a suggestion of the stress parameter decreasing with increasing **M** (this might have been more apparent if part B of the validation exercise had included larger **M** values). A stress parameter decreasing with **M** is consistent with a number of studies, such as Silva *et al.* (1996), Pezeshk *et al.* (2011), and N. Kuehn (written comm., 2014), although others explain the apparent decrease of $\Delta\sigma$ as a geometrical effect due to the finite size of the rupture (e.g., Baltay and Hanks, 2014).

The middle graph in Figure 10 shows a relatively clear **M** dependence for ε, similar to that in Atkinson and Silva (2000). We show a regression fit to the values, excluding the value from the Niigata earthquake. That fit is given by the equation

$$\log\varepsilon = 1.04 - 0.33\mathbf{M}. \tag{21}$$

ε decreases with increasing **M**. According to Figure 3, this may imply that the spectral sag is increasing with **M**. This, however, is conditional on the relation used for f_a (such as would be given by a relation similar to equation 15). For example, $\varepsilon = 0$ could be an SCF model if the $\Delta\sigma$ associated with f_a through equation (3) gives a high-frequency level consistent with the data.

The bottom graph in Figure 10 shows the finite-fault adjustment factor h. In addition to the values from our inversions, we also show values from Yenier and Atkinson (2014; hereafter YA14), which are generally consistent with our values. (We did not show their values of $\Delta\sigma$ and ε in the upper two graphs because YA14 assumed no crustal amplifications in their analysis, whereas we included crustal amplifications; this means that derived parameters that are strongly dependent on the absolute amplitudes of the simulated motions, such as $\Delta\sigma$, may be incompatible with our derived values. This problem should be less important for the parameter h, which is primarily dependent on the distance dependence of the spectra. For that reason, we only show the YA14 h values in Fig. 10.) There seems to be an **M** dependence of h, particularly if the one low value (from part A) is ignored. Most of the values of h from part A are in rough agreement with those from YA14. Until data from more events have been inverted for h, we suggest that the YA14 relations between h and **M** be used in forward simulations for all magnitudes, even those less than the lower limit of **M** 6 stated by YA14.
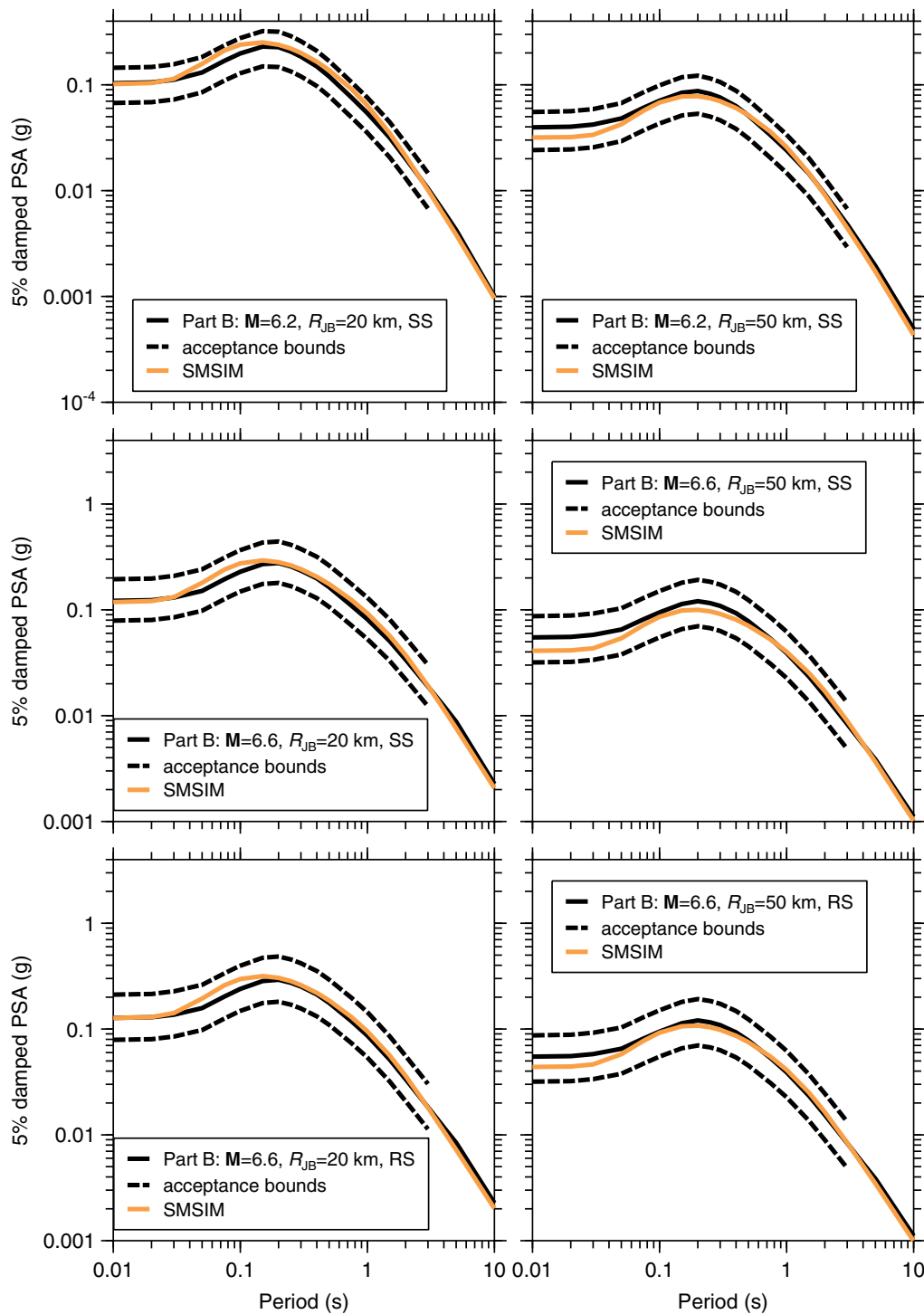
Figure 9. The median and acceptable bounds for PSA from recent ground-motion prediction equations (GMPEs) (part B), with the simulated PSA using parameters for the ADCF model inverted from the median part B PSA curves; see Table 1 for the parameters obtained from the inversions. As discussed in C. A. Goulet *et al.* (unpublished report, 2014; see Data and Resources), the solid black line in each graph shows the average median prediction from four Next Generation Attenuation-West 1 (NGA-West 1) GMPEs, summarized in Abrahamson *et al.* (2008). The dashed lines were obtained by considering the upper and lower bound of the GMPE predictions for the four models and the upper and lower bounds of the preliminary NGA-West 2 models in development as of 16 January 2013 (see Bozorgnia *et al.*, 2014, for a summary of the final GMPEs). A reference point was first specified by taking the largest GMPE prediction from all the models considered at any period. Fifteen percent was added to that maximum value. The upper-bound spectrum was then defined by applying the ratio of the upper-bound point to its corresponding median to the whole spectrum. The same process was applied for the lower-bound spectrum criterion. The color version of this figure is available only in the electronic edition.
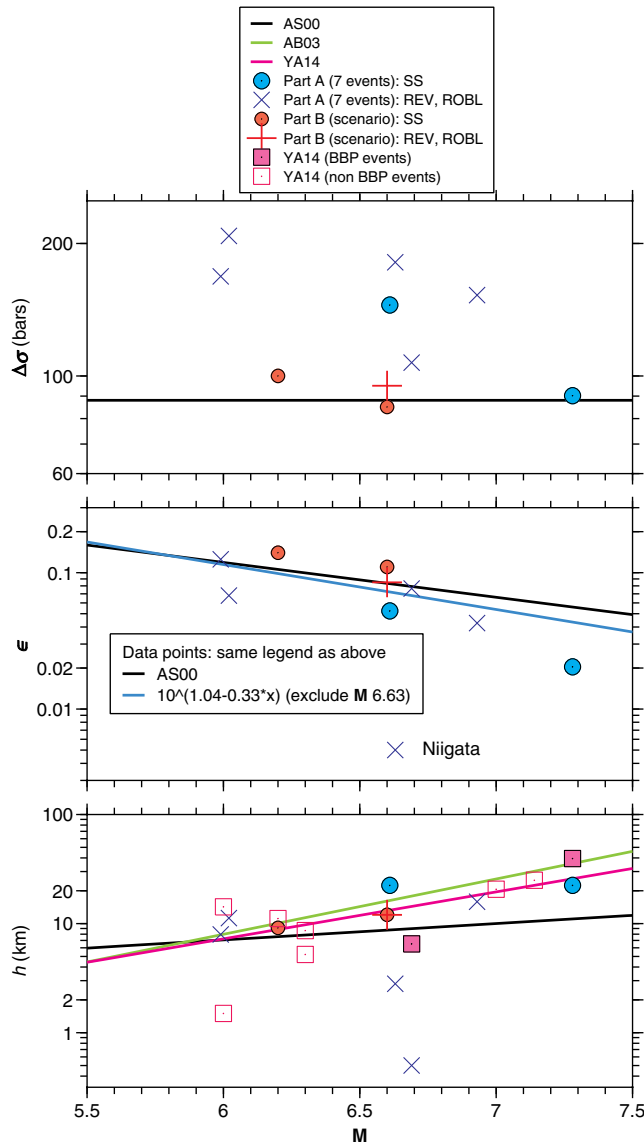
Figure 10. ADCF model source parameters derived from inversions of the part A and part B events. For reference, the value of the SCF model stress parameter that gives the same high-frequency spectral level as the Atkinson and Silva (2000; hereafter AS00) is given by the horizontal black line in the top graph. Also shown in the figure are the values of h from the analysis of Yenier and Atkinson (2014; hereafter YA14), as well as the h–M relations of AS00, Atkinson and Boore (2003; hereafter AB03), and YA14 (their relation is only for $M > 6$, but, as discussed in the text, we think it appropriate for smaller magnitudes). The color version of this figure is available only in the electronic edition.

Assuming that h is related to the dimensions of the fault-rupture surface, their relation, given by

$$\log h = -1.72 + 0.43\mathbf{M}, \tag{22}$$

gives realistically small values of h for small magnitudes. For example, for $\mathbf{M}$ 3, equation (22) gives $h = 0.4$ km, which is the same as the diameter of a circular rupture with a stress drop of 25 bars (larger values of the stress drop would give smaller
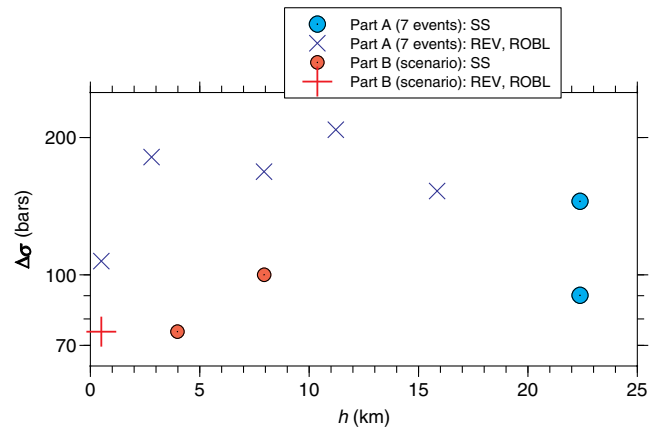
Figure 11. A scatterplot of $\Delta\sigma$ and h from the inversions of the Southern California Earthquake Center's Broadband Platform validation exercise events. There is no obvious correlation between $\Delta\sigma$ and h. The color version of this figure is available only in the electronic edition.

fault diameters). Although we would expect a mechanism-dependent h, because of differences in the aspect ratios of large strike-slip and reverse-slip faults, there are not enough data to determine one. Again, the analysis of more events is needed.

We might expect a trade-off in the inversions between h and $\Delta\sigma$, particularly if a significant number of observations used in the inversions are at close distances for which there will be a difference between the distances R and R_{RUP} (equation 19). The inversions for h and $\Delta\sigma$ are uncoupled if all the data are at distances for which $R_{RUP} \gg h$, for then $R \approx R_{RUP}$ and the amplitudes of the ground motion will be sensitive to $\Delta\sigma$ but not to h. A scatterplot of h and $\Delta\sigma$ (Fig. 11) shows no obvious correlation between the two.

Discussion and Conclusions

The generalized DCF ω^2 source models introduced here have enough flexibility in shape that they can be used to fit a wide range of data, while being constrained at low frequencies by the seismic moment and at high frequencies by the seismic moment M_0 (or equivalently, moment magnitude $\mathbf{M}$), and a stress parameter $\Delta\sigma$. Aside from these two parameters, two other parameters are needed to specify the shape of the spectra: either the corner frequency f_a or f_b and a weighting parameter ε.

The models were used in an inversion of data, assembled for the SCEC BBP validation exercise, to determine $\Delta\sigma$ and ε (and thus f_b) given f_a from a relation in Atkinson and Silva (2000). In addition, a finite-fault factor h was determined that helps account for finite-fault effects when simulating ground motions using the point-source stochastic method. The point-source model with the inverted parameters gave fits to response spectra that are comparable to and sometimes better than those from a number of finite-fault simulation models (e.g., Goulet, 2013). Although more data would need to be

inverted to constrain trends of the inverted parameters with **M**, we find a tendency for $\Delta\sigma$ and ε to decrease with **M** and h to increase with **M**. The trends for ε and h seem relatively robust; the overall trend for h is consistent with that found by YA14.

The inverted $\Delta\sigma$ values from part A of the BBP exercise were significantly higher than those from part B and suggest a decrease of $\Delta\sigma$ with increasing **M**. The part B exercise only considered magnitudes of 6.2 and 6.6, and thus $\Delta\sigma$ from part B cannot be used to assess a magnitude dependence for the stress parameter. On the other hand, the part B curves are based on an average of a large number of recordings from many earthquakes, and therefore source parameters obtained from inversions of the part B curves might be more useful for determining parameters for future simulations than those from part A. It would be useful in the future to determine the source parameters of the generalized DCF source model and the finite-fault adjustment factor h by fitting part B-type curves for a wider range of magnitudes and distances (but for which the GMPEs are well constrained) than are used in the SCEC BBP exercise.

Although we found that the ADCF model had sufficient flexibility in spectral shape to allow a good fit to the observations used in the SCEC BBP validation exercise, we have not had enough experience with the two generalized models introduced in this article to recommend one over the other. We offer the models here in the hope that future authors will find them useful in fitting observations with simulations.

Data and Resources

All but Figures 6–8 were prepared using CoPlot (www .cohort.com; last accessed July 2014). Version 3.80 of the Stochastic-Method SIMulation (SMSIM) programs was used in the validation process. The latest version of the SMSIM programs used for the simulations can be obtained from the online software link on http://www.daveboore.com (last accessed July 2014); their use is described in Boore (2005). The algorithm for interpolating two velocity profiles is given in *daves_notes_on_interpolating_two_given_velocity_profiles_ to_obtain_a_velocity_profile_with_specified_v30_v1.0.pdf*, available from www.daveboore.com/daves_notes.html (last accessed July 2014). The unpublished reports by D. S. Dreger *et al.* (2014), *Validation of the SCEC broadband platform V14.3 simulation methods using pseudo spectral acceleration data* and C. A. Goulet, N. A. Abrahamson, P. G. Somerville, K. E. Wooddell (2014), *The SCEC broadband platform validation exercise: 1 methodology for code validation in the context of seismic hazard analyses* were submitted to *Seismological Research Letters*.

Acknowledgments

References

Abrahamson, N., G. Atkinson, D. Boore, Y. Bozorgnia, K. Campbell, B. Chiou, I. M. Idriss, W. Silva, and R. Youngs (2008). Comparisons of the NGA ground-motion relations, *Earthq. Spectra* **24,** 45–66.

Atkinson, G. M. (1993). Earthquake source spectra in eastern North America, *Bull. Seismol. Soc. Am.* **83,** 1778–1798.

Atkinson, G. M., and D. M. Boore (1995). Ground motion relations for eastern North America, *Bull. Seismol. Soc. Am.* **85,** 17–30.

Atkinson, G. M., and D. M. Boore (2003). Empirical ground-motion relations for subduction zone earthquakes and their application to Cascadia and other regions, *Bull. Seismol. Soc. Am.* **93,** 1703–1729.

Atkinson, G. M., and W. Silva (2000). Stochastic modeling of California ground motions, *Bull. Seismol. Soc. Am.* **90,** 255–274.

Baltay, A. S., and T. C. Hanks (2014). Understanding the magnitude dependence of PGA and PGV in NGA-West 2 data, *Bull. Seismol. Soc. Am.* **104,** (in press).

Boore, D. M. (1983). Stochastic simulation of high-frequency ground motions based on seismological models of the radiated spectra, *Bull. Seismol. Soc. Am.* **73,** 1865–1894.

Boore, D. M. (1986). Short-period *P*- and *S*-wave radiation from large earthquakes: Implications for spectral scaling relations, *Bull. Seismol. Soc. Am.* **76,** 43–64.

Boore, D. M. (2003). Prediction of ground motion using the stochastic method, *Pure Appl. Geophys.* **160,** 635–676.

Boore, D. M. (2005). SMSIM—Fortran Programs for Simulating Ground Motions from Earthquakes: Version 2.3—A Revision of OFR 96-80-A, *U. S. Geol. Surv. Open-File Rept. 00-509*, revised 15 August 2005, 55 pp.

Boore, D. M. (2009). Comparing stochastic point-source and finite-source ground-motion simulations: SMSIM and EXSIM, *Bull. Seismol. Soc. Am.* **99,** 3202–3216.

Boore, D. M. (2013). The uses and limitations of the square-root impedance method for computing site amplification, *Bull. Seismol. Soc. Am.* **103,** 2356–2368.

Boore, D. M. (2014). What do data used to develop ground-motion prediction equations tell us about motions near faults? *Pure Appl. Geophys.* **171,** doi: 10.1007/s00024-013-0748-9.

Boore, D. M., and W. B. Joyner (1997). Site amplifications for generic rock sites, *Bull. Seismol. Soc. Am.* **87,** 327–341.

Bozorgnia, Y., N. A. Abrahamson, L. Al Atik, T. D. Ancheta, G. M. Atkinson, J. W. Baker, A. Baltay, D. M. Boore, K. W. Campbell, B. S.-J. Chiou, R. Darragh, S. Day, J. Donahue, R. W. Graves, N. Gregor, T. Hanks, I. M. Idriss, R. Kamai, T. Kishida, A. Kottke, S. A. Mahin, S. Rezaeian, B. Rowshandel, E. Seyhan, S. Shahi, T. Shantz, W. Silva, P. Spudich, J. P. Stewart, J. Watson-Lamprey, K. Wooddell, and R. Youngs (2014). NGA-West 2 Research Project, *Earthq. Spectra* **30,**, doi: 10.1193/072113EQS209M.

Brune, J. N. (1970). Tectonic stress and the spectra of seismic shear waves from earthquakes, *J. Geophys. Res.* **75,** 4997–5009.

Brune, J. N. (1971). Correction, *J. Geophys. Res.* **76,** 5002.

Goulet, C. (2013). SCEC BBP Validation Parameters: SCEC Ground Motions and Recommended Models for Use, presented at *The 2013 COSMOS Technical Session*, Emeryville, California, 22 November 2013, http://www.cosmos-eq.org/technicalsession/index.html, last accessed April 2014.

Hanks, T. C., and H. Kanamori (1979). A moment magnitude scale, *J. Geophys. Res.* **84,** 2348–2350.

Hanks, T. C., and R. K. McGuire (1981). The character of high-frequency strong ground motion, *Bull. Seismol. Soc. Am.* **71,** 2071–2095.

Hough, S. E., J. G. Anderson, J. Brune, F. Vernon III, J. Berger, J. Fletcher, L. Haar, T. Hanks, and L. Baker (1988). Attenuation near Anza, California, *Bull. Seismol. Soc. Am.* **78,** 672–691.

Joyner, W. B. (1984). A scaling law for the spectra of large earthquakes, *Bull. Seismol. Soc. Am.* **74,** 1167–1188.

Pezeshk, S., A. Zandieh, and B. Tavakoli (2011). Hybrid empirical ground motion prediction equations for eastern North America using NGA models and updated seismological parameters, *Bull. Seismol. Soc. Am.* **101,** 1859–1870.

Raoof, M., R. B. Herrmann, and L. Malagnini (1999). Attenuation and excitation of three-component ground motion in southern California, *Bull. Seismol. Soc. Am.* **89,** 888–902.

Silva, W. J., N. Abrahamson, G. Toro, and C. Costantino (1996). Description and validation of the stochastic ground motion model, *Final Report, Contract No. 770573*, Brookhaven National Laboratory, Associated Universities, Inc. Upton, New York, 1176 pp., http://pacificengineering.org/bnl/Bnl_rpt.zip (last accessed March 2014.)

Toro, G. R. (2002). Modification of the Toro et al. (1997) attenuation relations for large magnitudes and short distances, *Risk Engineering, Inc.* report, http://www.riskeng.com/downloads/attenuation_equations (last accessed May 2014).

Yenier, E., and G. M. Atkinson (2014). Equivalent point-source modeling of moderate- to-large magnitude earthquakes and associated ground-motion saturation effects, *Bull. Seismol. Soc. Am.* **104,** 1458–1478.

U.S. Geological Survey
MS 977
345 Middlefield Road
Menlo Park, California 94025
boore@usgs.gov
(D.M.B.)

GeoPentech, Inc.
525 N. Cabrillo Park Drive
Suite 280
Santa Ana, California 92701
Carola_DiAlessandro@geopentech.com
(C.D.A.)

Pacific Gas and Electric Company
245 Market Street
San Francisco, California 94117
naa2@pge.com
(N.A.A.)